JGR Space Physics

RESEARCH ARTICLE
10.1029/2025JA034418

Stormtime Magnetospheric Processes Associated With the Dawnside Current Wedge

S. Ohtani[1], S. Raptis[1], A. P. Devanandan[2], T. Motoba[1], Y. Zou[1], J. W. Gjerloev[3], and V. G. Merkin[1]

[1]Johns Hopkins University Applied Physics Laboratory, Laurel, MD, USA, [2]University of New Hampshire, Durham, NH, USA, [3]Catholic University of America, Washington, District of Columbia, USA

Key Points:

- As the dawnside auroral electrojet (AEJ) intensifies, geosynchronous B field dipolarizes, and its LT sector expands dawnward from the nightside
- During the intensification of the dawnside AEJ, magnetic reconnection is active in the dawnside plasma sheet with an X line retreating tailward
- Earthward reconnection outflow may be deflected dawnward by a dipolar B configuration sustaining the dawnward expansion of the current wedge

Correspondence to:
S. Ohtani,
ohtani@jhuapl.edu

Citation:
Ohtani, S., Raptis, S., Devanandan, A. P., Motoba, T., Zou, Y., Gjerloev, J. W., & Merkin, V. G. (2025). Stormtime magnetospheric processes associated with the dawnside current wedge. *Journal of Geophysical Research: Space Physics*, *130*, e2025JA034418. https://doi.org/10.1029/2025JA034418

Received 12 JUL 2025
Accepted 7 NOV 2025

Abstract The intensification of the westward auroral electrojet (AEJ) in the dawn sector is a characteristic feature of the storm main phase. It is considered an ionospheric segment of a wedge-type current system, the dawnside current wedge (DCW), formed by the disruption (short-circuiting through the ionosphere) of a magnetospheric equatorial current. The present study observationally investigates associated magnetospheric processes with a focus on near-Earth dipolarization and tail magnetic reconnection. It is found that as the dawnside AEJ intensifies, (a) geosynchronous magnetic field dipolarizes in the dawn sector, with its region expanding eastward from the nightside, and (b) tail reconnection becomes active in the dawnside plasma sheet, with an X line retreating tailward as suggested by negative-to-positive transitions of $V_{\perp,X}$ and B_z. (a) suggests that the DCW initially develops as a substorm current wedge expanding from the nightside. (b) implies that the corresponding dipolarization region expands dawnward as earthward reconnection outflows transport magnetic flux from the plasma sheet. It is suggested that the DCW develops following an enhancement of ionospheric conductance due to the precipitation of energetic electrons, which drift eastward after being injected by a nightside substorm. As the magnetic configuration becomes more dipolar, earthward reconnection outflows may be deflected farther dawnward, which possibly sustains the dawnward expansion of the DCW. At the same time, however, the pile-up of magnetic flux may lead to the retreat of the X line. Therefore, the DCW likely evolves as a consequence of a complex two-way coupling between the near-Earth current reduction and tail reconnection.

1. Introduction

During geomagnetic storms, the westward auroral electrojet (AEJ) very often intensifies in the dawn sector. Ohtani (2021) reported that its intensity is highly correlated with the dawn-dusk asymmetry of midlatitude magnetic depression, a characteristic feature of stormtime ground magnetic disturbances, which was initially attributed to the intensification of the duskside ring current (i.e., the partial ring current model) but subsequently debated (Crooker & Siscoe, 1974; Cummings, 1966; Fukushima & Kamide, 1973). It seems that the intensified AEJ often closes with a downward field-aligned current (FAC) in the morning sector, and with an upward FAC at postmidnight (Ohtani, Gjerloev, et al., 2018), although the actual local-time range probably varies from event to event. The local-time confinement of the AEJ intensification strongly suggests that it reflects the formation of a wedge-shaped current system, which may be considered as a magnetospheric equatorial current short-circuiting through the ionosphere. Its magnetospheric segment is probably either the ring current or the tail current. This current system is akin to the substorm current wedge on the nightside, and therefore, it may be referred to as dawnside current wedge (DCW). In this paper, we use the term "dawnside" in a loose sense to distinguish this current system from the conventional substorm current wedge, which usually forms on the nightside. In reality, the longitudinal structure and development of the DCW still remain to be understood.

The dawnside westward AEJ is generally considered as a Hall current corresponding to sunward return convection. However, Ohtani et al. (2023) found that during geomagnetic storms, the dawnside AEJ intensifies typically for 1–2 hr, often repeatedly, without any clear correlation with the sequence of external driving. Furthermore, the intensification is very often preceded by substorm activity in the midnight sector. Based on these features, they suggested that substorm injection of energetic electrons and subsequent enhancement of ionospheric conductance are crucial for the stormtime intensification of the dawnside AEJ. They also identified three other causes (i.e., enhanced convection, solar-wind compression, and the formation of a substorm current wedge in the dawn sector), which, however, are not prevalent.

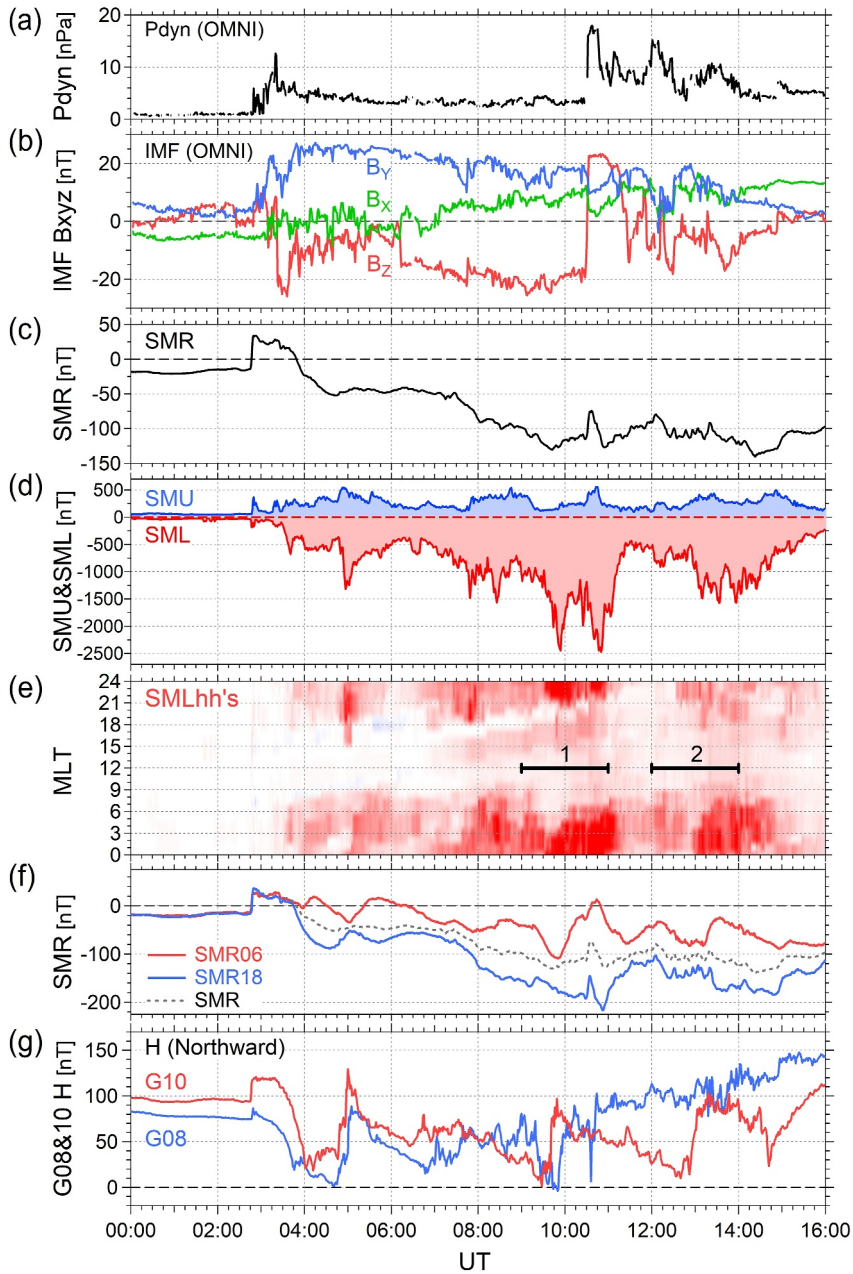

Figure 1. (a) Solar wind dynamic pressure, P_{dyn}, (b) IMF B_X (green), B_Y (blue), B_Z (red), (c) SMR, (d) SMU (blue) and SML (red) indices, (e) SMLhh's, (f) SMR06 (red), SMR18 (blue), and SMR (black dotted), and (g) G08 (blue) and G10 (red) H component during the 16-hr interval from 0000 UT to 1600 UT on 18 February 1999. The P_{dyn} and IMF data were taken from the OMNI database, for which the original measurements made by the ACE satellite near the L1 point were propagated to the subsolar bow shock. The two horizontal segments denoted as "1" and "2" in (e) show the intervals examined in Sections 2.2 and 2.3, respectively.

The dawnward progression of AEJ intensification can be naturally attributed to the magnetic drift of injected electrons. More specifically, those electrons drift eastward after injection, with some precipitating into the ionosphere through wave-particle interactions, thereby enhancing the ionospheric conductance. Accordingly, more magnetospheric current short-circuits through the ionosphere, intensifying the AEJ in the corresponding sector; this idea is schematically illustrated in Figure 11 as part of the summary of the present study. In fact, global auroral images show that the dawnside AEJ intensifies as the region of intense aurora emission expands dawnward, supporting this idea. This model predicts that the geosynchronous magnetic field dipolarizes first on

the nightside in association with the substorm and then its region expands dawnward as a manifestation of the development of the DCW.

Interestingly, Raptis et al. (2024) recently reported that during the storm main phase, plasma-sheet convection is more enhanced on the dawnside than on the duskside compared with non-storm periods. In addition, Sorathia et al. (2023) showed, with a global model, that the DCW grows as reconnection becomes active in the dawnside plasma sheet with its earthward outflows reaching the dawnside near-Earth region. Therefore, it is vital to observationally address whether and how tail magnetic reconnection develops during the dawnside AEJ intensification. Such an investigation may strengthen the aforementioned model of the DCW development, which does not incorporate tail magnetic reconnection.

The objective of the present study is to systematically investigate, for the first time, magnetospheric signatures observed in association with the stormtime intensification of the dawnside AEJ. A particular focus is placed on geosynchronous dipolarization and fast plasma flows in the plasma sheet. Here geosynchronous dipolarization can be considered a manifestation of the DCW, whereas fast plasma-sheet flows are indicative of active tail reconnection if B_Z changes consistently. We observationally examine how these phenomena are organized in time and space relative to the intensification of the dawnside AEJ and discuss the development of the DCW in the context of tail dynamics.

The rest of this paper is organized as follows. In Section 2, we examine example events of the dawnside AEJ intensification using satellite magnetometer and plasma measurements along with global auroral images and ground magnetic field data. In Section 3, we statistically examine the spatiotemporal development of geosynchronous dipolarization and tail reconnection referring to the start of the dawnside AEJ intensification. We discuss the results in Section 4, and summarize the present study in Section 5.

2. 18 February 1999 Storm

2.1. Overview of the Storm Main Phase

In this section, we examine the intensification of the dawnside westward AEJ observed during two distinct intervals on 18 February 1999. Earlier on that day, an interplanetary shock arrived (Figure 1a) followed by a prolonged period of strongly southward (<−20 nT) IMF B_Z (Figure 1b). The storm sudden commencement (SSC) of this storm was marked by a sharp increase in SMR in at 0246 UT (Figure 1c). SMR is the SuperMAG equivalent of the conventional Dst index but derived from the 1-min averages of northward ground magnetic disturbances measured at all available stations at |MLat (magnetic latitude)| ≤ 50° (Newell & Gjerloev, 2012). SMR reached a minimum of ∼−130 nT at 0943 UT, when IMF B_Z was at lowest levels before it sharply turned northward at 1030 UT. However, northward IMF B_Z lasted only for ∼1 hr, and as IMF B_Z became southward again, SMR reached another minimum of ∼−140 nT at 1423 UT and then started to recover. We chose this storm event for a close examination because (a) two GOES satellites were located in the postmidnight-to-early morning sector, (b) the Geotail satellite stayed in the dawnside plasma sheet, and (c) global auroral images taken by the Polar satellite are available.

Figure 1d shows the SMU and SML indices, which are the SuperMAG equivalents of the AU and AL indices, respectively (Newell & Gjerloev, 2011); these indices are derived from data obtained in 40° < MLat < 80°, and accordingly, they serve as measures of the (maximum) eastward and westward AEJs even when the auroral oval expands equatorward during geomagnetic storms. During this storm, the westward AEJ intensified significantly with SML almost reaching −2,500 nT. In contrast, SMU stayed mostly below 500 nT. The predominance of the westward AEJ can be attributed to strongly positive IMF B_Y (Figure 1b) (e.g., Burch et al., 1985; Weimer, 2005). For several distinct intervals, SML became below −1,000 nT. Especially for those after 0730 UT, the westward AEJ intensified mostly in the midnight-to-dawn sector as shown by SMLhh's in Figure 1e; SMLhh's are the subindices of SML derived from data within 3 hr in MLT centered at MLT = hh.

In Figure 1f, we plot SMR06 (red) and SMR18 (blue) along with SMR (black dotted). SMR06 and SMR18 are subindices of SMR derived from data in the corresponding MLT quadrant, SMR06 for dawn and SMR18 for dusk. SMR18 continued to be more negative than SMR06, which reflects the dawn-dusk asymmetry of stormtime (main phase) magnetic depression. Every time the dawnside AEJ intensified, SMR06 increased, but SMR18 decreased. This is common for the stormtime intensification of the dawnside AEJ, and can be explained in terms of the DCW (Ohtani, 2021; Ohtani et al., 2023). The northward ground magnetic component increases inside the wedge,

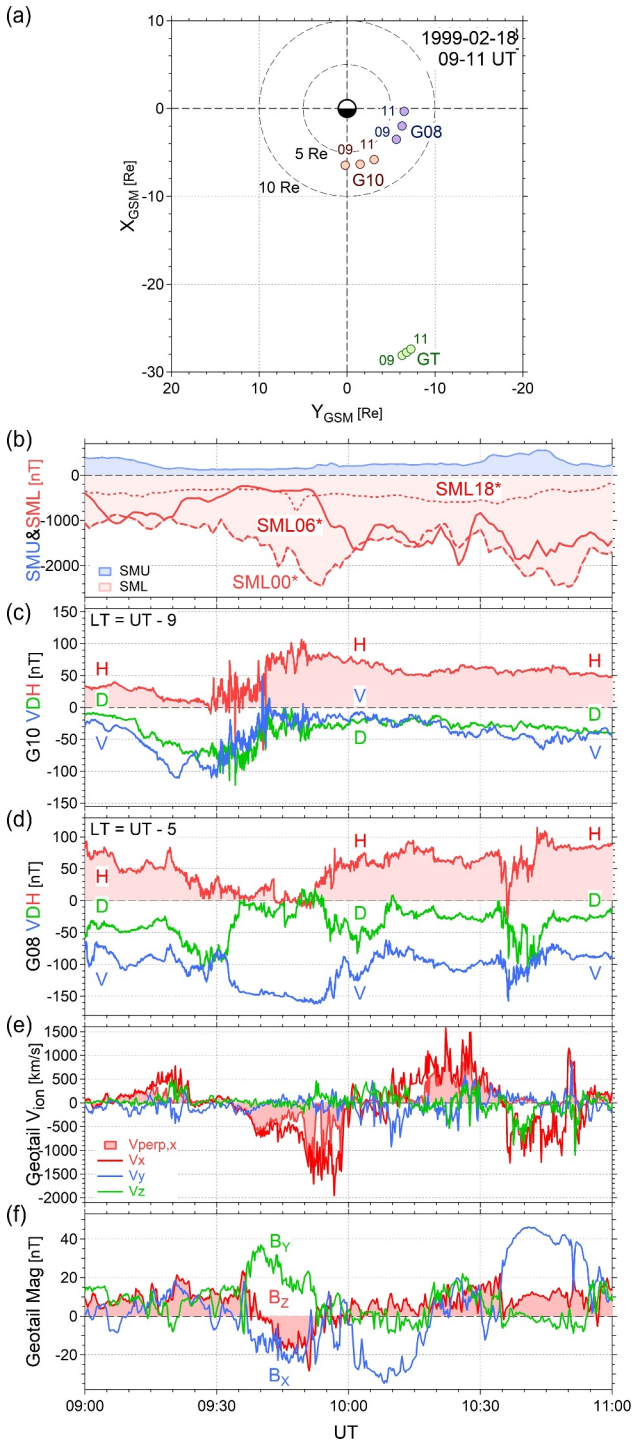

Figure 2. (a) Locations of G08, G10, and Geotail (GT) in X_{AGSM}–Y_{AGSM}, (b) SMU (shaded in blue) and SML (shaded in red) along with SML00* (dashed), SML06* (solid), and SML18* (dotted), (c) G10 and (d) G08 magnetic field measurements in *VDH*, Geotail (e) ion velocity and (f) magnetic field measurements in GSM for the 2-hr interval from 0900 to 1100 UT on 18 February 1999.

whereas it decreases outside. This idea is analogous to the substorm current wedge causing northward magnetic disturbances (i.e., positive bay) inside but southward outside (Clauer & McPherron, 1974; Ohtani et al., 2021). However, whereas the substorm current wedge usually extends in the midnight sector, the DCW is centered at much later MLTs.

Dipolarization is an expected magnetospheric feature of the DCW (Section 1). In fact, in the present event, the GOES 08 (G08) and 10 (G10) geosynchronous satellites observed, in the postmidnight-to-dawn sector, that the *H* (northward) component increased when the dawnside AEJ intensified (Figure 1g). In the following subsections, we examine in detail the spatiotemporal evolution of geosynchronous dipolarization and the associated tail dynamics.

2.2. The Interval of 0900–1100 UT

First, we examine the interval of 0900–1100 UT on 18 February 1999; the interval is marked by a horizontal bar (denoted as "1") in Figure 1e. Figure 2b shows the sequences of SML (lightly shaded in red) and SMU (lightly shaded in blue) along with SMLhh*'s in different line styles; each SMLhh* is the same as SMLhh but derived from ground station data within a 6-hr window, rather than a 3-hr window, in MLT. SML was already around −1,000 nT before 0930 UT, then decreased further by 1,500 nT in 20 min. This SML reduction can be attributed to the intensification of the westward AEJ in the midnight sector as indicated by SML00* (dashed line) tracing SML. Around the peak of SML00*, however, SML06* (solid line) started to decrease from above −500 nT to below −1,500 nT catching up SML as SML00* recovered, which suggests that the center of the westward AEJ moved dawnward. In contrast, its duskward expansion was limited as indicated by the lack of noticeable reduction of SML18* (dotted line), which, however, may be partly attributed to the sparse distribution of ground stations in the duskside auroral zone as will be shown next.

Figure 3 shows the SuperMAG polar map of ground magnetic disturbances (green vectors) on the top of global auroral images taken by the Visible Imaging System (VIS) of the Polar satellite (Frank et al., 1995) every 15 min from 0925 to 1040 UT. The ground magnetic disturbances are rotated clockwise by 90° so that their distribution serves as a proxy of equivalent currents (but in units of nT). The Polar auroral images captured only a partial view of the polar region as the satellite was not positioned high enough in altitude, and accordingly, the imager's line of sight was skimming the polar ionosphere. The westward AEJ intensified along with auroral emission in the midnight sector (Figures 3a and 3b), which initially expanded more clearly duskward than dawnward (Figure 3c). Then, the duskward expansion halted, and the westward AEJ started to weaken at premidnight by 1010 UT (Figure 3d). In contrast, the dawnward expansion became more pronounced, and both the westward AEJ and auroral emission intensified over the entire midnight-to-dawn sector (Figures 3e and 3f).

Figures 2c and 2d show the *VDH* magnetic components observed by GOES 10 (G10) and 8 (G08), respectively. *VDH* represents a cylindrical coordinate system, where *H* (red) is parallel to the dipole axis positive northward, *V* is perpendicular to *H* positive outward, and *D* completes a right-handed orthogonal system pointing eastward. Whereas G10 was located at postmidnight (LT = UT − 9), G08 was located at early dawn (LT = UT − 5) during the interval (Figure 2a).

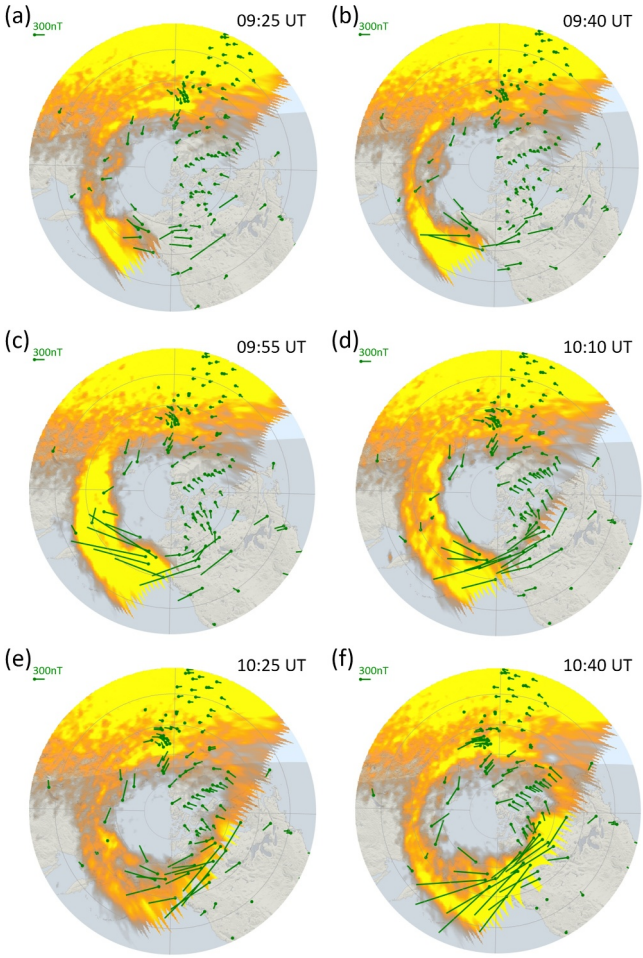

Figure 3. Polar diagrams of ground magnetic disturbances (green arrows rotated clockwise by 90°) along with Polar VIS auroral images at (a) 0925, (b) 0940, (c) 0955, (d) 1010, (e) 1025, and (f) 1040 UT on 18 February 1999.

For G10 (Figure 2c), the increase in H (shaded in red) starting around 0928 UT was most noticeable. It started with large fluctuations, but after ~0940 UT, H remained at a sustained level. Along with the H increase, V (blue) also increased (its magnitude decreased). Note that before these increases, both H and V tended to decrease for a few tens of minutes. That is, the local magnetic field was stretched and then dipolarized, and each component changed with a magnitude (~100 nT) comparable to the total dipole magnetic field at geosynchronous orbit. Presumably, this dipolarization reflected the unloading of significant energy, and was associated with the aforementioned intensification of the westward AEJ in the midnight sector. A similarly large dipolarization was observed at G08 but starting at 0952 UT, 24 min later than at G10, and 4 hr later in MLT. Apparently, the dipolarization region expanded dawnward, which is consistent with the dawnward expansion of the AEJ intensification. The expansion speed, 1 hr in MLT per 6 min, is also consistent with the visual inspection of the spatial development of the AEJ intensification.

During this interval, the Geotail satellite was in the dawnside plasma sheet (Figure 2a), and measured plasma (Mukai et al., 1994) and magnetic field (Kokubun et al., 1994). Figure 2e shows three ion velocity components along with the X component of the velocity perpendicular to the local magnetic field, $V_{\perp,X}$ (shaded in red), and Figure 2f shows three magnetic components. V_X was the dominant component during most of the interval. Roughly speaking, V_X turned negative (tailward) at ~0925 UT, and the flow continued to be tailward for ~25 min. Then, after a short period of transition, V_X became positive (earthward) at ~1010 UT, and the flow continued to be earthward for ~30 min. Throughout this tailward-then-earth flow sequence, the flow was very often directed perpendicular to the local magnetic field as indicated by $V_X \approx V_{\perp,X}$, and its speed occasionally exceeded 1,000 km/s.

During the same interval, each magnetic component changed systematically. In particular, B_Z (shaded in red) became strongly negative in the middle of the tailward flow interval, and then after turning positive, increased gradually with fluctuations while the flow was directed continuously earthward. The overall sequence of the B_Z and V_X variations can be well interpreted in terms of magnetic reconnection. An X line initially formed earthward of Geotail around 0930 UT, retreated tailward passing the Geotail X distance, and stayed farther down the tail; an alternative interpretation is that two distinct X lines formed successively, first earthward and then tailward of Geotail, which, however, is less plausible as we will discuss later. Note that the reconnection was apparently active for over 1 hr, during which the dipolarization region expanded dawnward from postmidnight to early dawn as observed by G10 and G08 (Figures 2c and 2d). We therefore conclude that during this event, the dawnward expansion of the geosynchronous dipolarization region was sustained by magnetic flux transport by the continuously active magnetic reconnection in the plasma sheet.

Finally, we point out that Geotail observed another burst of tailward flow starting at 1035 UT, which lasted at least 15 min. The satellite was located off the equatorial plane as indicated by large magnitudes of B_X (blue line in Figure 2f), and accordingly, the observed tailward flow was basically field-aligned. Nevertheless, it is possible that this tailward flow was caused by a new X line that formed on the earthward side of Geotail. Around the start of this tailward flow, G08 observed at dawn (LT = ~5.7) a sharp reduction of the H component followed by a sharp and large two-step increase (Figure 2d). In addition, as we saw earlier, the westward AEJ intensified significantly with its east front reaching the dawn meridian (Figure 3f). It is therefore plausible that the later intensification of the westward AEJ reflected a distinct reconnection event in the plasma sheet. At postmidnight (LT = ~1.7), G10 did not observe any clear signature of dipolarization (Figure 2c). It is suggested that for this second reconnection, the associated earthward outflow, an expected counterpart of the observed tailward flow, deflected farther dawnward, and transported magnetic flux to a later MLT sector than for the earlier reconnection. This feature may be essential for the development of DCW, as we will discuss in Section 4.

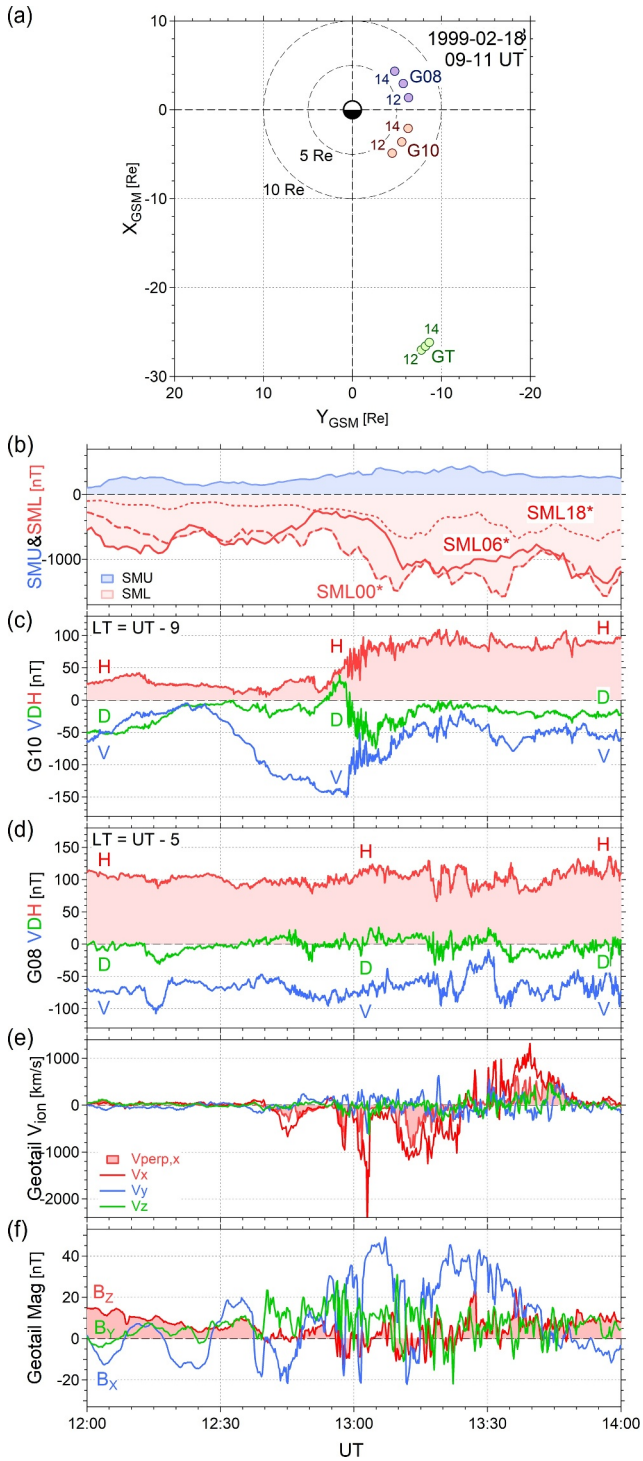

Figure 4. The same as Figure 2 but for the interval from 1200 to 1400 UT on 18 February 1999.

2.3. The 2nd Interval of 1200–1400 UT

Next, we examine the intensification of the westward AEJ during the interval of 1200–1400 UT on 18 February 1999, as marked by the horizontal bar (denoted as "2") in Figure 1e. Figure 4b shows that starting at 1255 UT, SML00* decreased from −560 to −1,490 nT in 15 min. SML06* started to decrease 10 min later, meeting SML00* at ∼−1,100 nT. We therefore conclude that the westward AEJ started to intensify in the midnight sector and then expanded dawnward.

This sequence of the AEJ intensification can be confirmed in Figure 5, which shows ground magnetic disturbances and Polar auroral images from 1225 to 1315 UT. The polar map at 1235 UT shows an intensification of auroral emission at premidnight (Figure 5b), which evolved into a large auroral bulge extending over the entire midnight sector, and the westward AEJ also intensified (Figures 5a–5d). The auroral bulge continued to expand both duskward and dawnward. The westward AEJ intensified from postmidnight to dawn in MLT, whereas its duskward extension was ambiguous partly due to the sparse distribution of ground stations.

Around 1300 UT, G10 was at ∼04 LT (Figure 4a), and observed a large (∼80 nT) increase in H following an unusually large (∼150 nT) reduction of V. That is, the local magnetic field changed from a very stretched to a more dipolar configuration. In contrast, at ∼08 LT, G08 did not observe any clear signature of dipolarization. The contrast of magnetic signatures at G10 and G08 presumably reflected their location relative to the DCW, as inferred from the MLT extent of the AEJ intensification. Specifically, G10 was located inside, but G08 was outside the DCW.

At 1300 UT, Geotail was in the dawnside plasma sheet, slightly earthward and dawnward of its position during the 1st interval (Figure 4a). After 1240 UT, Geotail frequently observed fast plasma flows (Figure 4e), and large fluctuations of B_X and B_Y with their signs alternating frequently (Figure 4f). Accordingly, the observed fast flows were often field-aligned (as inferred from the difference between V_X and $V_{\perp,X}$). Two negative spikes of V_X were observed immediately before and after 1300 UT, when the dipolarization was in progress at G10. Another fast tailward flow started 7 min later. V_X was persistently negative and large for the next 15 min, followed by a period of equally persistent but positive V_X. Throughout the entire interval, B_Z tended to be negative for fast tailward flows, and positive for fast earthward flows. It is therefore suggested that those flows were caused by magnetic reconnection, and the reconnection site was located earthward of Geotail during the intensification of the dawnside westward AEJ and then retreated tailward. The overall sequence of geosynchronous dipolarization and tail reconnection during this second interval was very similar to what we found for the first interval (Section 2.2).

3. Statistical Study

3.1. Event Selection

In this section, we statistically examine magnetospheric signatures observed during the intensification of the dawnside AEJ. Using the SMR index from 1996 to 2024, we identified 805 storm intervals requiring that SMR reached −50 nT or less. For each SMR minimum, the storm interval was defined as the period from the last instance SMR was above −10 nT prior to the SMR minimum to the first instance it exceeded −10 nT after the minimum; see Ohtani (2021) for more details. We then searched for SML06* reductions by sliding, through each storm interval, a 4-hr window with 1-min

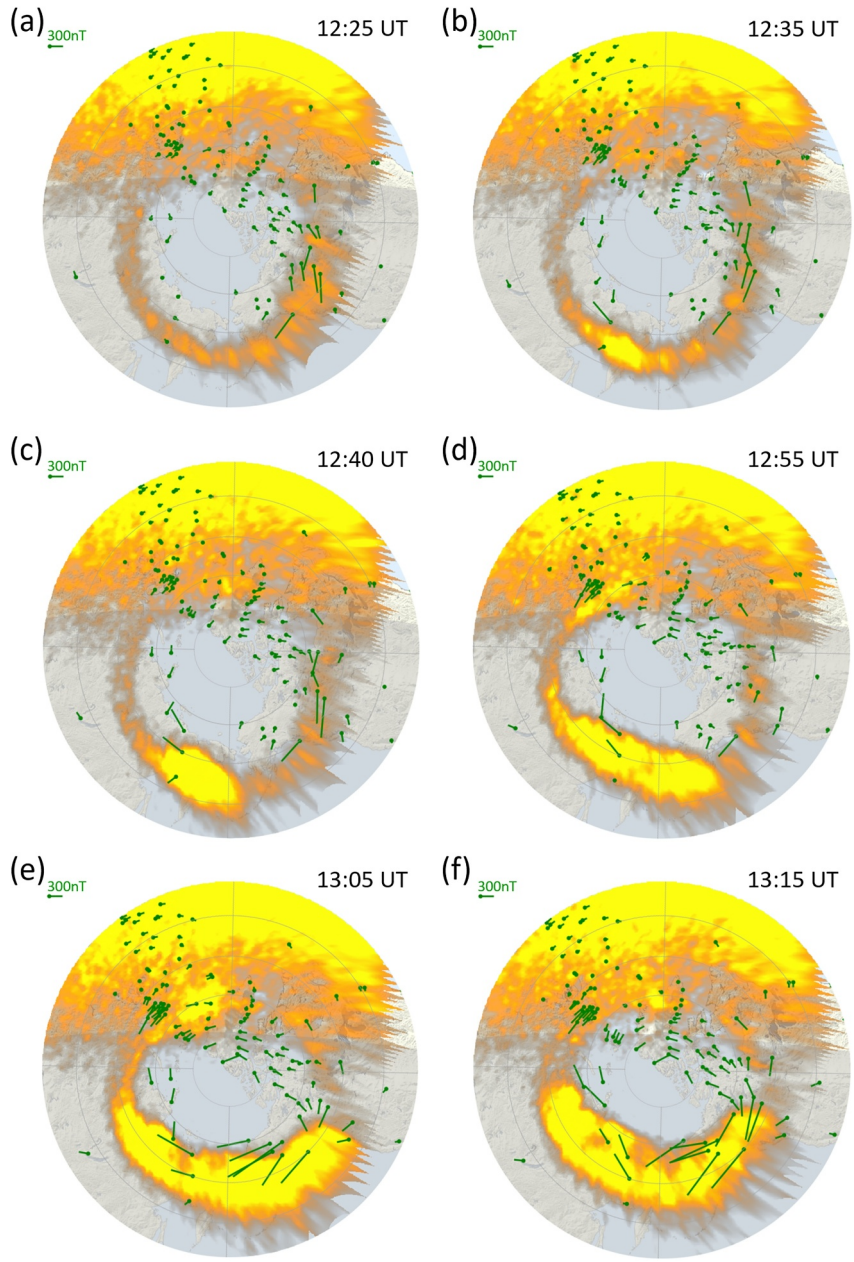

Figure 5. The same as Figure 3 but for (a) 1225, (b) 1235, (c) 1240, (d) 1255, (e) 1305, and (f) 1315 UT on 18 February 1999. No Polar auroral image is available at 1245 UT, and therefore, the polar map at 1240 UT is shown instead in (c).

increments. If the value of SML06* at the center of the window was the minimum and below −1,000 nT, we considered the interval as a candidate event and recorded it with the center time $t = T_P$.

Then, following Ohtani et al. (2023), we applied a linear fit to SMR06 for $T_P - 2\ \text{hr} \le t \le T_P$, and identified the start of each event, T_S, as the point where ΔSMR06, the deviation of SMR06 from the fit, attains its minimum value. This idea is similar to identifying substorm onset with the start of midlatitude positive bays. Note, however, that ΔSMR06 increases not only due to the formation of a new current wedge but also due to the expansion of a pre-existing current wedge from the nightside to the dawn quadrant. We required ΔSMR06 ≤−10 nT at T_S. Finally, we visually inspected the sequences of SML06* and SMRhh's and excluded questionable events (e.g., ULF oscillations, and global compression). We selected 439 events in total. The distribution of event UT hours is shown in Figure A1a of Appendix A, and discussed in terms of the longitudinal nonuniformity of auroral-zone ground stations.

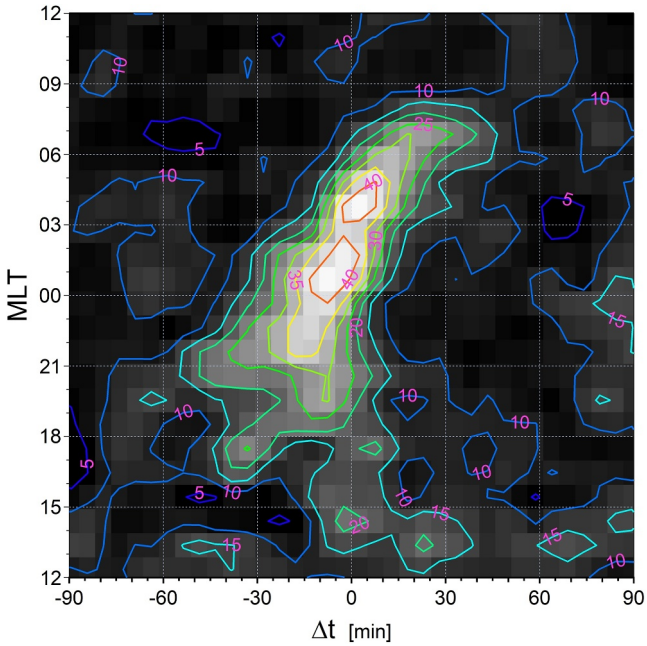

Figure 6. Occurrence probability (%) of geosynchronous dipolarization in MLT versus Δt.

3.2. Geosynchronous Dipolarization

First, we examine the occurrence and spatial development of geosynchronous dipolarization by examining 1-min averages of the H component measured by various GOES satellites, from GOES-8 to -18. Figure 6 presents the occurrence probability of dipolarization in percent in MLT versus Δt ($= t - T_S$). Here, we consider that the geosynchronous magnetic field dipolarized if H increased by more than 15 nT compared to 20 min earlier. For each 20-min window, the MLT and Δt at the midpoint were used to create this probability map. The counts of 20-min windows are shown in Figure A1b of Appendix A. The count values vary by approximately a factor of two across the domain but generally fall within the range of 500–1,100, providing sufficient statistical confidence in discussing the spatiotemporal development of dipolarization.

In Figure 6, the equi-contours of high probability extend over many hours in MLT from premidnight at $\Delta t < 0$ to morning at $\Delta t > 0$. They are centered around $\Delta t = 0$ at MLT = 00–04 with a peak probability exceeding 40%. That is, around the start of the dawnside AEJ intensification, the geosynchronous magnetic field often dipolarizes at MLTs from postmidnight to early dawn, which is preceded by dipolarization in the midnight sector. There may exist another segment of equi-contours, which extends westward from premidnight but with significantly lower probabilities.

Since the occurrence probability is generally high, and its equi-contours reveal a coherent structure, it is plausible that Figure 6 captures the essence of the actual spatial development of the dipolarization region. More specifically, preceding the dawnside AEJ intensification, the geosynchronous magnetic field often dipolarizes in the midnight sector, and then its region expands predominantly dawnward along with the AEJ intensification. From the slope of the contours, the expansion speed is estimated at 1 hr (in MLT)/5 min; it takes 5 min to expand 1 hr in MLT. This estimate is consistent with the expansion speed that we estimated from the time difference in dipolarization between G08 and G10 in Section 2.2. The sequence of dipolarization is also consistent with the statistical tendency that the westward AEJ intensifies first in the midnight sector and then in the dawn sector (Ohtani et al., 2023). Dipolarization and the intensification of the westward AEJ are manifestations of substorms. We therefore conclude that the DCW initially develops as the substorm current wedge expands from the nightside.

3.3. Fast Flows and B_Z in the Plasma Sheet

Next, using Geotail data, we examine plasma-sheet signatures observed in association with the intensification of the dawnside AEJ. The Geotail orbit changed since it was launched in 1992, but for the period of the storms that we selected from 1996 onward, its apogee and perigee distances were around 31 and 9–10 R_E, respectively. We focus on the area $X_{AGSM} \le -10\ R_E$ and $-15 \le Y_{AGSM} \le +15\ R_E$; here, X_{AGSM} and Y_{AGSM} are X and Y coordinates in the GSM system aberrated by 4°. We consider that Geotail was in the plasma sheet if $\beta_i \ge 0.5$ (β_i: the ratio of the ion thermal pressure to the magnetic pressure), $|B_Z| \ge B_{XY}/2$ ($B_{XY} = \sqrt{B_X^2 + B_Y^2}$), and $N \le 2\ \mathrm{cm}^{-3}$ (N: ion number density). The requirement for N excludes measurements in the magnetosheath and the low-latitude boundary layer.

Figures 7a and 7b show Geotail orbital segments in X_{AGSM}–Y_{AGSM} and Z^*_{GSM}–Y_{AGSM}, respectively; Z^*_{GSM} is defined as $Z_{GSM} - 8 \times \sin(\theta_{dip})$ (θ_{dip}: dipole tilt angle), which may be considered as a measure of satellite distance from the neutral sheet assuming that the neutral sheet hinges at 8 R_E; in reality, the hinging distance varies in a complex way depending on external conditions (Tsyganenko & Fairfield, 2004). The segments when Geotail was in the aforementioned nightside area at $-60 \le \Delta t$ ($= t - T_S$) $\le +60$ min are shown in gray, while those in the plasma sheet are highlighted in red. Geotail was often in the plasma sheet when it was at $|Z^*_{GSM}| < 5\ R_E$ in the dawnside magnetotail. On the duskside, in contrast, the orbital segments spread more widely in Z^*_{GSM}, and furthermore, the satellite was less frequently in the plasma sheet even at $|Z^*_{GSM}| < 5\ R_E$. Accordingly, Geotail provided very limited data for the duskside plasma sheet.

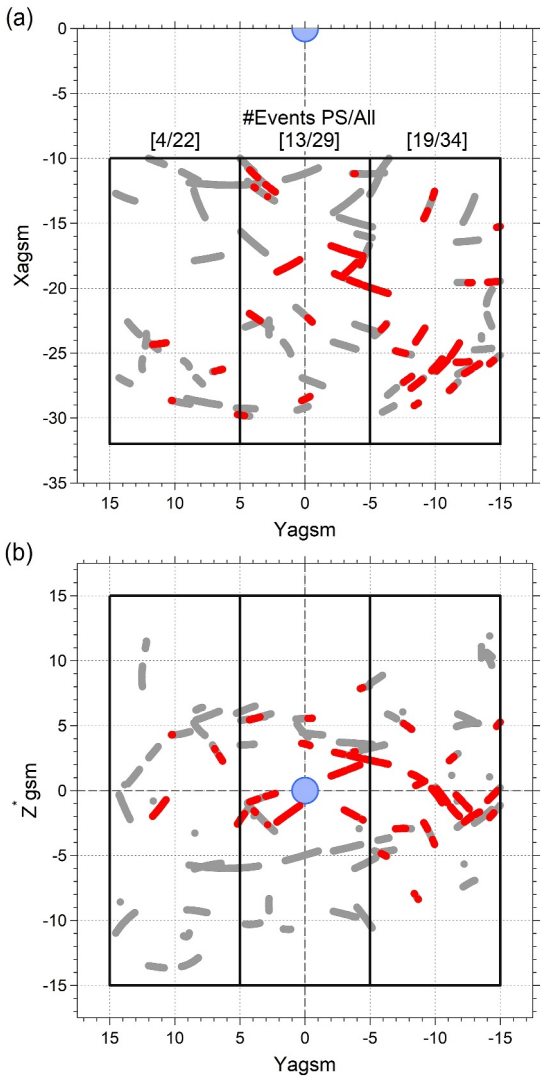

Figure 7. Geotail orbital segments during the selected intensifications of the dawnside AEJ in (a) X_{AGSM}–Y_{AGSM} and (b) Z^*_{GSM}–Y_{AGSM}. The segments when Geotail was in the plasma sheet are highlighted in red. The three boxes in each panel represent the duskside, midnight, and dawnside regions that are examined separately. The numbers in brackets at the top of each box in (a) indicate the number of events in which Geotail was present in the plasma sheet, and the total number of events in the corresponding region.

Now we examine three regions of the magnetotail separately, duskside ($+5 < Y_{AGSM} \leq +15\ R_E$), near midnight ($-5 \leq Y_{AGSM} \leq +5\ R_E$), and dawnside ($-15 \leq Y_{AGSM} < -5\ R_E$) as framed in Figure 7. Each box extends from -10 to $-32\ R_E$ in X_{AGSM}, and we consider all plasma-sheet data points irrespective of Z^*_{GSM}. Figures 8a–8c show, as a function of $\Delta t = t - T_S$, $V_{\perp,X}$ measured in the duskside, midnight, and dawnside plasma sheets, respectively. Figures 8d–8f show B_Z in the same way. Different colors indicate different events, providing an idea of how many events reveal similar or different features.

Except for the dawnside plasma sheet, it is difficult to confidently address any specific feature due to the limited number of events. This is especially the case for the duskside plasma sheet (Figures 8a and 8d). For the midnight plasma sheet, we can find negative B_Z spikes $\Delta t \leq +20$ min (Figure 8e), some of which are coincident with negative spikes of $V_{\perp,X}$ (Figure 8b), suggesting the formation of an X line earthward of the spacecraft. In contrast, at $\Delta t > +20$ min, B_Z is persistently positive (Figure 8e). These features seem to be consistent with the sequence of tail reconnection in the dawnside plasma sheet, which we address next.

Our focus is on the results for the dawnside plasma sheet (Figures 8c and 8f). Despite significant scattering, both $V_{\perp,X}$ and B_z appear to follow a certain pattern. For $V_{\perp,X}$, points are scattered more positively than negatively at $-60 < \Delta t < -30$ min, but predominantly negatively at $-20 < \Delta t < +20$ min. Then, large positive points stand out again at $\Delta t > 30$ min. The overall sequence of B_Z seems to be similar to that of $V_{\perp,X}$. B_Z is predominantly positive at $-60 < \Delta t < -30$ min, but negative points become more noticeable as we approach the reference time (i.e., $\Delta t = 0$). Then, B_Z becomes predominantly positive again after $\Delta t = 10$ min. We note that whereas both $V_{\perp,X}$ and B_z reveal positive-negative-positive transitions over more than 1 hr, extreme points are often aligned vertically indicating that their changes tend to be spiky.

Figure 9 shows B_Z against $V_{\perp,X}$ for the dawnside subset of the Geotail plasma-sheet measurements in the same color code as Figures 8c and 8f. Many points are distributed around the positive vertical axis indicating that $|V_{\perp,X}|$ is small (<100 km/s) for most of the data points, but B_Z varies significantly reflecting the magnetic field at various locations of various configurations. Most importantly, points with extreme values of $V_{\perp,X}$ and B_Z scatter primarily in the 1st and 3rd quadrants. That is, B_Z tends to be positive for fast earthward flows, and negative for fast tailward flows, as we generally expect for the outflows of tail magnetic reconnection. Here, for the combination of $V_{\perp,X} < 0$ and $B_Z < 0$, the reconnection site lies earthward of the spacecraft, and for $V_{\perp,X} > 0$ and $B_Z > 0$, it lies tailward of the spacecraft.

The fact that both $V_{\perp,X}$ and B_Z tend to be strongly negative around $\Delta t = 0$ min (Figures 8c and 8f) suggests that around the start of the dawnside AEJ intensification, magnetic reconnection was active earthward of Geotail. There are five events (as marked in different colors in Figure 8f) in which Geotail observed fast tailward flows at $-20 < \Delta t < +20$ min. In those five events, Geotail was located at -20.1, -23.6, -25.7, -27.4, and $-27.5\ R_E$ in X_{AGSM}, not distinctly far tailward compared to the entire plasma sheet events (Figure 7a); the median X_{AGSM} of the 19 events was $-24.5\ R_E$. Therefore, the observed tendency for fast flows to be directed tailward suggests that the corresponding reconnection site was located closer to Earth during this particular interval.

However, there are only five such events, and in Figures 8c and 8f, data points are distributed so densely around the horizontal axis that individual events cannot be distinguished. For addressing the scatter of the data points, we plot in Figures 10a and 10b the median (solid magenta) and lower (25%) and upper (75%) quartiles (dashed

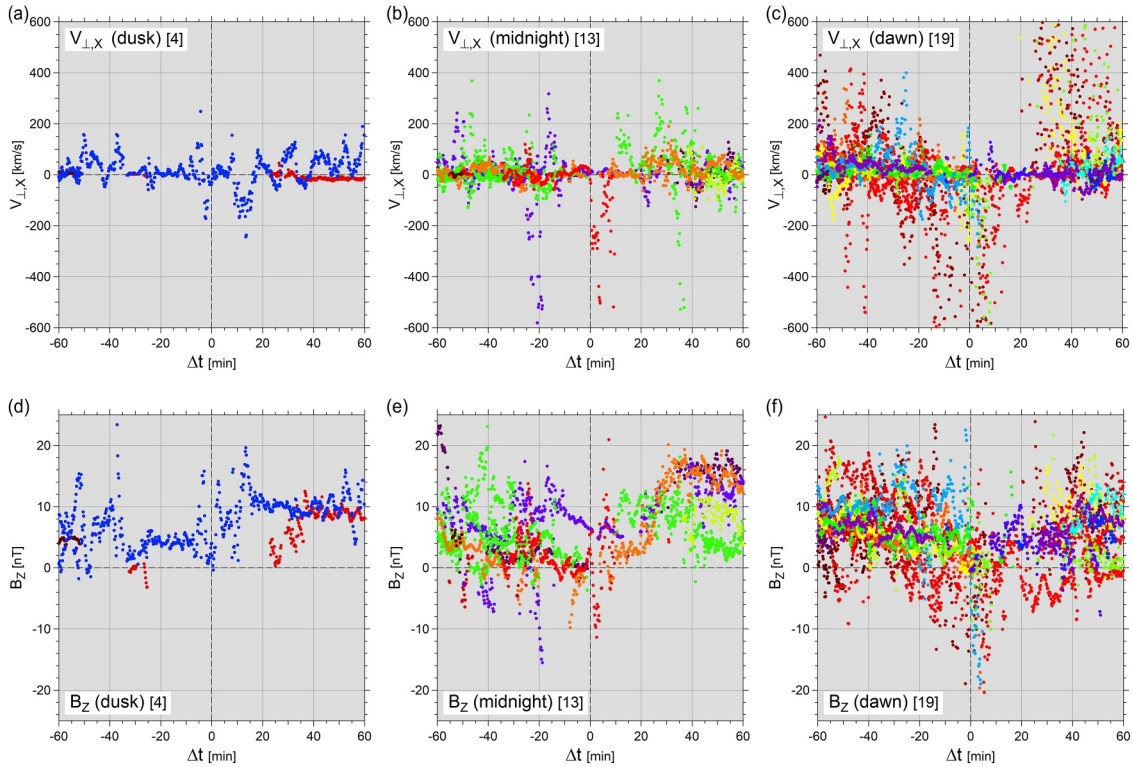

Figure 8. Geotail measurements of (top) $V_{\perp,X}$ and (bottom) B_Z for the (left) duskside, (middle) midnight, and (right) dawnside plasma sheet during the selected intensifications of the dawnside AEJ as a function of Δt in different colors for different events.

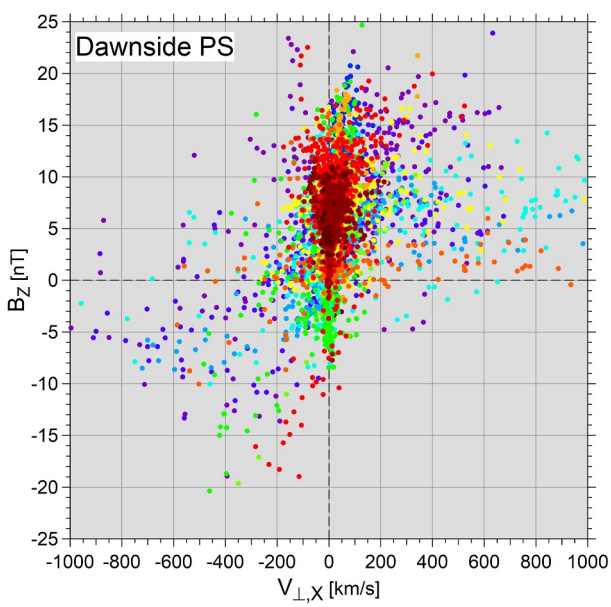

Figure 9. B_Z versus $V_{\perp,X}$ measured by Geotail in the dawnside plasma sheet during the selected intensifications of the dawnside AEJ. Different colors represent different events following the same color scheme as Figures 8c and 8f.

magenta) of $V_{\perp,X}$ and B_z, respectively, along with the original data points (gray dots). In Figure 10a, the median and quartiles of $|V_{\perp,X}|$ are also plotted in black.

Compared to Figure 8c, Figure 10a reveals a slightly different sequence. That is, the interval of fast tailward flows is clearly centered at $\Delta t > 0$ min. At $\Delta t < -10$ min, the quartiles of both $V_{\perp,X}$ and $|V_{\perp,X}|$ are small in magnitude, indicating that flows are slow for the predominant majority of the data points. Then, $V_{\perp,X}$ becomes biased negatively, and its median and lower quartile reach their minima (i.e., tailward) at $+5 < \Delta t < +10$ min, before reverting to positive (i.e., earthward) peaking at $\Delta t = \sim 30$ min (Figure 10a). This tailward-to-earthward flow reversal coincides with the reduction of B_Z with the minimum of its lower quartile almost reaching -5 nT at $0 < \Delta t < +10$ min (Figure 10b), when the lower quartile of $V_{\perp,X}$ reaches -400 km/s. Thus, the overall sequence is consistent with the previously mentioned idea that the active reconnection site retreats tailward passing the Geotail X distance, but Figures 10a and 10b suggest more clearly that the process tends to concur with the intensification of the westward AEJ in the dawn sector.

Interestingly, during the same interval, the numbers of plasma sheet events and data points drop significantly. Figure 10c shows the numbers of events (red; scaled on the left axis) and data points (blue; scaled on the right axis) in each 5-min bin, with solid lines for the plasma sheet and dashed lines for the entire tail. Here, if an event has at least one plasma-sheet data point in a 5-min bin, it is counted as a plasma-sheet event for that particular bin. Since the resolution of the data is 12 s, there would be 25 (=5 min × 5 points/min) data points if the satellite continuously stays in the plasma sheet for 5 min. The

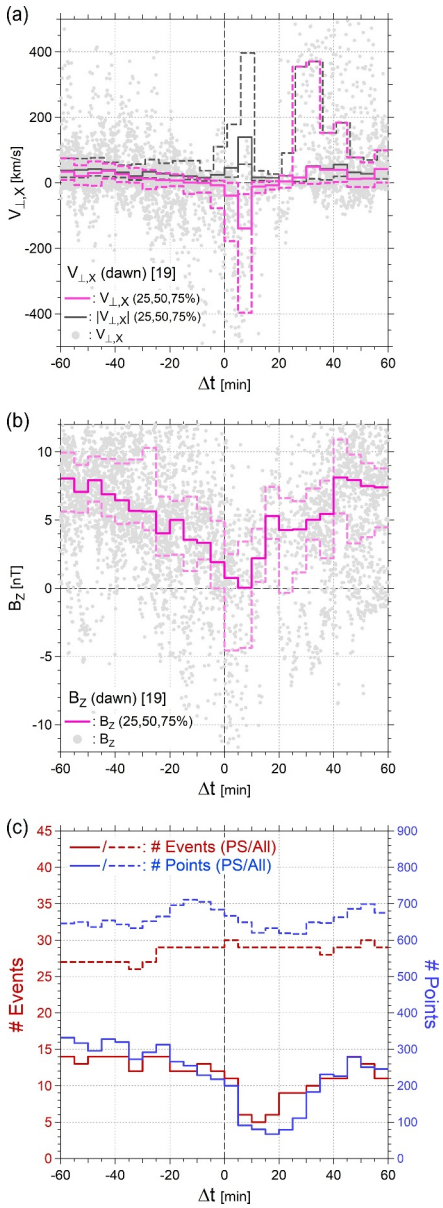

Figure 10. (a) The median (magenta solid), and lower and upper quartiles (magenta dashed) of $V_{\perp,X}$, along with those of $|V_{\perp,X}|$ (black) measured by Geotail in the dawnside plasma sheet. The original measurements are shown by gray dots. (b) The same as (a) but for B_Z. (c) The numbers of the dawnside AEJ intensification events with Geotail in the dawnside plasma sheet (red solid) and magnetotail (red dashed) scaled on the left axis, and the numbers of Geotail data points in the dawnside plasma sheet (blue solid) and magnetotail (blue dashed) in those events scaled on the right axis.

actual ratio is roughly 20; note that the scale of the right axis is 20 times larger than that of the left axis. The numbers of plasma-sheet events (red solid) and plasma-sheet data points (blue solid) have a dip at $+5 < \Delta t < +30$ min even though the total numbers of events (red dashed) and data points (blue dashed) basically remain constant. The dip may be traced back in time to $\Delta t = -10$ min, and forward to +40 min, extending over the aforementioned interval of the negative-to-positive transition of $V_{\perp,X}$ and B_z (Figures 10a and 10b). Apparently, the satellite tends to be outside of the plasma sheet during the corresponding period, which suggests that the plasma sheet is thinner. This result supports the aforementioned idea that the active X line retreats tailward during the course of the dawnside AEJ intensification.

4. Discussion

4.1. Geosynchronous Dipolarization

In this study, we examined magnetospheric signatures observed during the stormtime intensification of the dawnside AEJ. We found that the geosynchronous magnetic field often dipolarizes as the dawnside AEJ intensifies, which strongly suggests that the enhanced dawnside AEJ is an ionospheric segment of a wedge current system, the DCW, with a magnetospheric current (partially) short-circuiting through the ionosphere. This magnetospheric current can be either the tail current or the ring current. Distinguishing between them is not essential for the following discussion, but the associated current reduction occurs primarily outside of geosynchronous orbit; otherwise, the geosynchronous H component would not increase. We also found that the dipolarization region very often expands eastward from the midnight sector. The result is consistent with the idea that the DCW wedge initially develops as the substorm current wedge expands dawnward from the nightside, following an enhancement of ionospheric conductance due to the precipitation of eastward-drifting energetic electrons (Section 1). This idea is schematically shown in Figure 11 along with the associated tail dynamics, which we will discuss in the next subsection.

However, the relationship between the DCW and the substorm current wedge is a complex issue. First, it still remains to be understood, even for non-stormtime substorms, whether the substorm current wedge consists of two wedges, one at premidnight and another at postmidnight (Gjerloev & Hoffman, 2014). It is appealing to consider that the DCW is actually this postmidnight part of the substorm current wedge but disconnected and enhanced extremely due to intense stormtime precipitation. In addition, attributing the dawnside AEJ intensification to conductance enhancement assumes the presence of an underlying electric field, which is probably a part of global convection driving a sunward return flow and significantly enhances during geomagnetic storms. Therefore, it is plausible that as long as the ionospheric conductance remains elevated, the DCW is sustained even after the initial substorm decays.

An important question is why the dipolarization region expands more distinctly dawnward than duskward. Note that in non-stormtime substorms, geosynchronous dipolarization expands both eastward and westward from the onset meridian, but more notably westward (Nagai, 1982). In fact, the westward expansion of dipolarization seems to be an inherent feature of substorm evolution. It corresponds to the westward expansion of the substorm current wedge with an intense upward FAC at its front (e.g., Kepko et al., 2015), which is widely considered as the magnetospheric counterpart of the westward traveling surge, an essential feature of auroral substorms (Akasofu, 1964; Fujii et al., 1994; Gjerloev & Hoffman, 2014).

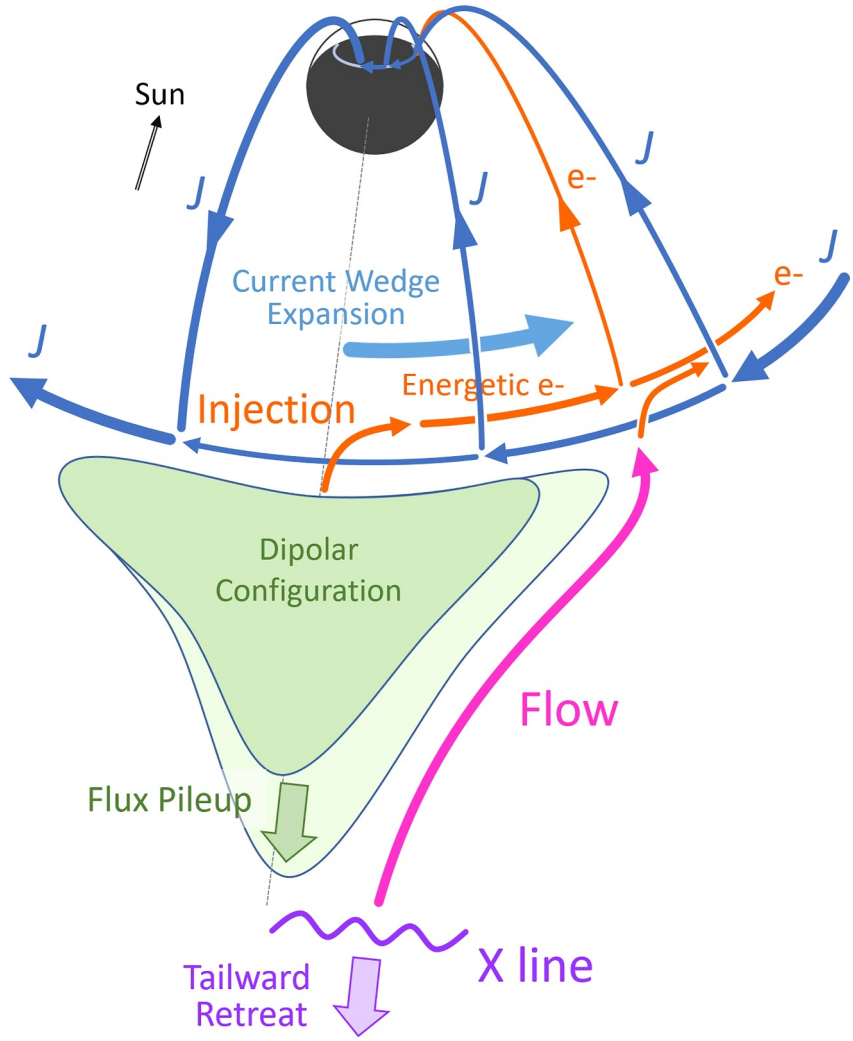

Figure 11. Schematic explanation of the dawnward expansion of the DCW.

Interestingly, Ohtani, Motoba, et al. (2018) investigated sharp dipolarizations observed inside geosynchronous orbits, which are typically associated with geomagnetic storms. They selected, as sharp dipolarizations, events with an H increase by at least 10 nT in 1 min, in contrast to 15 nT in 20 min as we did in Section 3.2. These events exhibit a distinctly duskward-skewed occurrence distribution, which along with a similar distribution of dispersionless injections (Motoba et al., 2021), suggests the preferred occurrence of substorm onset location in the premidnight sector. Furthermore, sharp dipolarizations propagate preferably westward rather than eastward. The contrast of the result of the present study to these observations suggests that there exists a distinct stormtime process, or a stormtime state of the magnetosphere, that favorably facilitates gradual dipolarizations and their dawnward expansion. This point is closely related to the issue that we discuss next, that is, the role of tail reconnection in the development of the DCW.

4.2. Near-Earth Reconnection

In this subsection, we discuss how the near-Earth reconnection, more specifically its earthward outflow, is related to geosynchronous dipolarization, and how, or if, it contributes to the development of the DCW. In general, fast earthward flow in the plasma sheet more often does not lead to geosynchronous dipolarization than it does (Ohtani et al., 2006), which can be explained in terms of the equilibrium point of the interchange motion of depleted flux tubes (i.e., low pV^{γ}) located outside of geosynchronous orbit (Dubyagin et al., 2010; Kim et al., 2012; Wolf et al., 2009). However, we found in Section 3.3 that in association with the intensification of the dawnside AEJ,

tail magnetic reconnection is often active, and the plasma sheet tends to be in a distinct state as suggested by the prolonged negative-to-positive transition of $V_{\perp,X}$ and B_Z along with the thinning of the plasma sheet. This result strongly suggests that there is a certain causal link between the tail reconnection and the development of the DCW, for which there are two possibilities.

First, it is possible that the active reconnection is an effect of the DCW. The magnetospheric segment of the DCW is the reduction of a westward current. Whereas it causes dipolarization closer to Earth, it reduces equatorial B_Z on the tailward side, which is favorable for the formation of an X line. This idea naturally explains why tail reconnection is active primarily after the intensification of the dawnside AEJ (Section 3.3). The idea is similar to the inside-out scenario of substorm initiation (e.g., Lui, 1991) except that the associated reduction of the magnetospheric current is possibly driven by the enhancement of ionospheric conductance rather than an internal instability of the plasma sheet.

Another possibility is that the tail reconnection is the cause of the development of the DCW. This idea has some similarities to a popular substorm initiation model, the outside-in model, which proposes that the substorm current wedge forms because the earthward reconnection outflow is decelerated as the background magnetic field becomes more dipolar (e.g., Shiokawa et al., 1998). However, one crucial difference is that for the dawnside AEJ intensification, the reconnection is active mostly after, rather than before, its initiation. Therefore, the primary role of tail reconnection may be to sustain the dawnward expansion of the dipolarization region by transporting magnetic flux to its eastern front.

However, whereas the dawnward expansion of the geosynchronous dipolarization region appears to be systematic, fast plasma-sheet flows are generally bursty in time (e.g., Angelopoulos et al., 1994) and localized in the dawn-dusk direction (Sergeev et al., 1996). The obvious question is how the systematic large-scale feature (i.e., the eastward expansion of the DCW) could result from the sporadic local process (i.e., tail reconnection).

First, the dipolarization region might expand dawnward because the reconnection site moves dawnward in the plasma sheet. As mentioned earlier, the DCW reduces equatorial B_Z on its tailward side, which is favorable for tail reconnection. Therefore, it is possible that as the current wedge expands dawnward, the region of reduced equatorial B_Z also expands dawnward and so does the reconnection site. However, in the 18 February 1999 event, Geotail observed fast flows intermittently but over 5 hr. In addition, the trajectories of earthward reconnection outflows can be complex (e.g., Merkin et al., 2019; Wiltberger et al., 2015). Therefore, it may not be realistic to consider that the destination of reconnection outflows systematically moves dawnward because the reconnection site moves dawnward.

Another possibility is that earthward reconnection outflows deflect farther dawnward as the DCW develops. During the storm main phase, tail equatorial B_Z is elevated due to the ring current intensification (Ohtani & Mukai, 2008). This effect may be more significant on the duskside (as injected ions drift duskward), suppressing tail reconnection in the duskside plasma sheet. In the dawnside plasma sheet, in contrast, the stormtime enhancement of convection reflects the increased frequency of fast flows (Raptis et al., 2024). It is therefore possible that during the storm main phase, tail reconnection is more active on the dawnside than on the duskside. This dawn-dusk asymmetry may be pronounced during the DCW formation, which is often preceded by a nightside substorm that leads to dipolarization in the midnight sector and ring current intensification on the duskside (due to injected energetic ions). The situation may be envisioned as a dipolar magnetic configuration in the midnight sector blocking the penetration of earthward outflows of dawnside tail reconnection, and as the dipolarization region expands dawnward, earthward reconnection outflows may be deflected farther dawnward as schematically illustrated in Figure 11. This idea is consistent with the geosynchronous magnetic field response to the fast tailward flow observed by Geotail after ~1035 UT during the February 1999 storm, the later distinct tailward flow during the first interval (Figure 2). Following this tailward flow, G08 observed dipolarization at dawn, but G10 did not at postmidnight, even though both G08 and G10 observed dipolarization for the preceding tailward flow. This result suggests that the associated earthward reconnection outflow, an expected counterpart of this later tailward flow, carried magnetic flux farther dawnward as expected.

In reality, however, the DCW may develop and decay as the near-Earth current reduction and tail reconnection affect each other. As mentioned earlier, the current reduction in the near-Earth region reduces the equatorial B_Z farther out and possibly facilitates tail reconnection. In contrast, the effects of earthward reconnection outflows may be complex. First, they carry magnetic flux leading to dipolarization in the near-Earth region. The carried

magnetic flux may pile up enhancing the equatorial B_Z farther out (Figure 11). This may be the reason why the X line retreats tailward after the AEJ intensifies in the dawn sector (Section 3.3). Earthward reconnection outflows also carry energetic electrons to the near-Earth region, some of which precipitate into the ionosphere, whether in the sector of injection or in a later MLT sector after drifting eastward, and enhance ionospheric conductance. Accordingly, more current would short-circuit through the ionosphere from the magnetosphere. Energetic ions are also injected, which drift westward intensifying the ring current (Sorathia et al., 2023). As a consequence, the equatorial B_Z may stay elevated around midnight but weaken on the dawnside, supporting the recurrent formation of the DCW. Thus, by transporting magnetic flux, electrons, and ions to the near-Earth region, tail reconnection may affect the development of the DCW, as well as its own, in a complex way.

One notable characteristic of the DCW is that the associated dipolarizations continue significantly longer than those observed at substorm onset in the midnight sector. This characteristic may suggest that tail reconnection in the dawnside plasma sheet is characterized differently for storm periods. In fact, for the 18 February 1999 storm, the negative-to-positive transitions of $V_{\perp,X}$, which consisted of successive bursty enhancements, lasted several tens of minutes. In general, plasma-sheet flow bursts last only a few minutes even during storm periods (Devanandan et al., 2024), but tail reconnection associated with the DCW development may intensify repetitively over much longer periods. It is also possible that the radial profile of pV^{γ} differs in the stormtime dawnside plasma sheet, leading to more gradual deceleration of earthward reconnection outflows, and therefore, to more gradual dipolarizations (as opposed to sharp dipolarizations due to sudden deceleration at a sharp transition between dipolar and stretched magnetic configurations). Exploring these possibilities is crucial for better understanding the development of the DCW.

The present study strongly suggests that the development of the DCW is a system-level process in stormtime geospace, facilitating coupling between different regions, such as the magnetosphere and ionosphere, as well as the plasma sheet and near-Earth magnetosphere. It also bridges different scales, linking large-scale dipolarizations with meso-scale plasma flows, as well as with small-scale wave-particle interaction for the conductance enhancement. We hope that the findings of this study will help establish a framework for understanding and addressing this complex yet essential stormtime process.

5. Summary

In this study, we examined magnetospheric signatures observed during the stormtime intensification of the dawnside AEJ, with a particular focus on near-Earth dipolarization and tail reconnection. In Section 2, we closely examined two intervals during the February 1999 storm. In Section 3, we statistically examined the spatial development of geosynchronous dipolarization, and the sequences of $V_{\perp,X}$ and B_z in the plasma sheet. These analyses led to consistent results. First, we found that the geosynchronous magnetic field dipolarizes in the dawn sector as the dawnside westward AEJ starts to intensify, which can be considered as a manifestation of the DCW. The associated dipolarization often starts earlier in the midnight sector. It is therefore suggested that the DCW initially develops as the substorm current wedge extends dawnward. The sequence is consistent with the idea that the DCW expands dawnward following the enhancement of ionospheric conductance due to the precipitation of energetic electrons, which drift eastward after being injected on the nightside. We also found that along with the intensification of the dawnside AEJ, tail reconnection becomes active in the dawnside plasma sheet. The associated X line forms in the near-Earth region and then retreats tailward slowly as suggested by the negative-to-positive transition of B_z and $V_{\perp,X}$ over several tens of minutes. It is proposed that due to a dipolar magnetic configuration at earlier MLTs, earthward reconnection outflows deflect dawnward, sustaining the eastward expansion of the dipolarization region. Whereas the near-Earth current reduction weakens equatorial B_Z in the plasma sheet possibly facilitating tail reconnection, the pile-up of transported magnetic flux enhances equatorial B_Z, which may cause the tailward retreat of the X line. It is therefore possible that the DCW develops as a consequence of complex two-way coupling between the near-Earth current reduction and tail reconnection.

Appendix A

Ground stations in the auroral zone are unevenly distributed, with dense coverage in some longitudinal sectors and sparse coverage in others (Section 2). In this appendix, we evaluate the influence of such spatial nonuniformity on our event selection, and examine its potential impact on the conclusions of the present study.

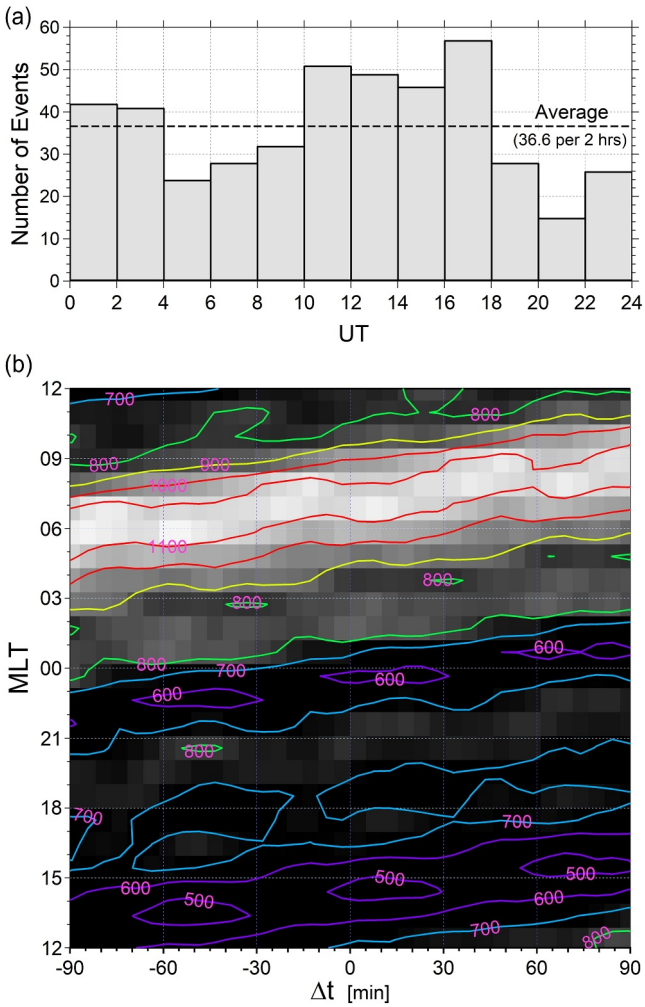

Figure A1. (a) Event count as a function of UT hour at the onset of dawnside current wedge formation, as defined in the manuscript. (b) Counts of 20-min GOES data windows, binned in 5-min × 1-hr ($\Delta t \times$ MLT), used to calculate the occurrence probability of dipolarization.

Figure A1a shows the event count as a function of UT hour at the onset of dawnside current wedge formation ($t = T_S$) for the 439 events that we, as well as Ohtani et al. (2023) examined. The primary hump extends from 10 UT to 18 UT. For this UT range, the dawnside auroral zone is densely covered by ground stations, as shown in Figures 3 and 5 in the main text, providing optimal coverage for detecting intensifications of the dawnside AEJ. In the dusk sector, in contrast, ground stations are distributed sparsely. There is a secondary, albeit minor, hump extending from 00 UT to 04 UT. For this UT range, the early-dawn sector is well covered by Scandinavian stations, which is favorable for detecting the expansion of the substorm current wedge from the midnight sector. Concurrently, North America is positioned at dusk, and ground stations are densely distributed in the dusk-side auroral zone.

Therefore, whereas intensifications of the duskside AEJ may be underrepresented for events in the primary hump (Section 2), the station distribution for events in the latter UT range is well suited for assessing whether the duskside AEJ intensifies in association with the DCW formation. Accordingly, the limited duskward expansion of the westward AEJ intensification relative to its more pronounced dawnward expansion (Ohtani et al., 2023) cannot be attributed to the nonuniform spatial distribution of auroral-zone ground stations.

In fact, the asymmetric expansion of the AEJ intensification can be independently inferred from the difference between the SMR06 and SMR18 sequences. Whereas SMR06 increases after the DCW formation, SMR18 decreases, contrary to the expectation that it would increase if the current wedge expands duskward in a similar way to its dawnward expansion (Figure 11 of Ohtani et al. (2023)). The reduction of SMR18 as well as the enhancement of SMR06 can be interpreted consistently as a remote effect of the DCW.

Since the locations of GOES satellites are fixed relative to Earth, the distribution of event UT hours directly influences their MLT distribution. Figure A1b shows the counts of 20-min GOES data windows binned in 5-min × 1-hr ($\Delta t \times$ MLT), which we used for calculating the occurrence probability of dipolarization (Figure 6). The overall ascending slope of the structures reflects Earth's rotation. The count values vary by approximately a factor of two across the domain but generally fall within the range of 500–1,100, providing sufficient statistical confidence in discussing the spatiotemporal development of dipolarization. Moreover, the high-probability dipolarization area in MLT versus Δt, as shown in Figure 6, exhibits a coherent structure, and our focus is on the expansion direction of the dipolarization region rather than its exact occurrence probabilities. Thus, our conclusion of the predominant dawnward expansion of the dipolarization region is supported with high confidence.

Conflict of Interest

The authors declare no conflicts of interest relevant to this study.

Data Availability Statement

SuperMAG indices, polar maps of ground magnetic disturbances, and magnetic field data at individual stations are available at the SuperMAG site (https://supermag.jhuapl.edu/). The OMNI data are available at the NASA OMNI website (https://omniweb.gsfc.nasa.gov/). Magnetometer data from GOES-16, -17, and -18 are available at https://www.ngdc.noaa.gov/stp/satellite/goes-r.html, and data from earlier GOES satellites (from GOES-08 to

GOES-15) are available at https://www.ncei.noaa.gov/products/satellite/goes-1-15. Geotail magnetometer and plasma data are available at https://darts.isas.jaxa.jp/app/stp/geotail/ascii.html.

Acknowledgments

We are most grateful to the members of the Center for Geospace Storms (CGS) team (https://cgs.jhuapl.edu/) for fruitful discussions. We also gratefully acknowledge that Geotail magnetometer data used in this study were provided by S. Kokubun and T. Nagai, and plasma data by T. Mukai and Y. Saito. GOES magnetometer data were provided by the National Centers for Environmental Information, National Oceanic and Atmospheric Administration (NOAA). We are also very grateful to the NSF SuperMAG facility. The SuperMAG indices and polar maps used in this study were derived from ground magnetometer data provided by many organizations and institutes as listed at https://supermag.jhuapl.edu/info/?page=acknowledgement. The Polar VIS global auroral images were originally provided by L. A. Frank and J. B. Sigwarth. This work was supported by the NASA DRIVE Science Center for Geospace Storms (CGS) under award 80NSSC22M0163. Work at APL was also supported by NSF Grant 2224986 (SO), NASA Grants 80NSSC21K0036 (SO), 80NSSC24K1113 (JWG, SO), 80NSSC24K0268 (TM), 80NSSC25K7676 (TM), 80NSSC25K0073 (TM), and the JHU/APL Independent R&D fund (SR).

References

Akasofu, S.-I. (1964). The development of the auroral substorm. *Planetary and Space Science*, *12*(4), 273–282. https://doi.org/10.1016/0032-0633(64)90151-5

Angelopoulos, V., Kennel, C. F., Coroniti, F. V., Pellat, R., Kivelson, M. G., Walker, R. J., et al. (1994). Statistical characteristics of bursty bulk flow events. *Journal of Geophysical Research*, *99*(A11), 21257–21280. https://doi.org/10.1029/94ja01263

Burch, J. L., Reiff, P. H., Menietti, J. D., Heelis, R. A., Hanson, W. B., Shawhan, S. D., et al. (1985). IMF B_y -dependent plasma flow and Birkeland currents in the dayside magnetosphere: 1. Dynamics Explorer observations. *Journal of Geophysical Research*, *90*(A2), 1577–1593. https://doi.org/10.1029/JA090iA02p01577

Clauer, C. R., & McPherron, R. L. (1974). Mapping the local time-universal time development of magnetospheric substorms using mid-latitude magnetic observations. *Journal of Geophysical Research*, *79*(19), 2811–2820. https://doi.org/10.1029/JA079i019p02811

Crooker, N. U., & Siscoe, G. L. (1974). Model geomagnetic disturbance from asymmetric ring current particles. *Journal of Geophysical Research*, *79*(4), 589–594. https://doi.org/10.1029/JA079i004p00589

Cummings, W. D. (1966). Asymmetric ring currents and the low-latitude disturbance daily variation. *Journal of Geophysical Research*, *71*(19), 4495–4503. https://doi.org/10.1029/JZ071i019p04495

Devanandan, A., Keesee, A. M., Katus, R. M., Tibbetts, J., Raptis, S., & Merkin, V. G. (2024). Statistical analysis of bursty bulk flows in the magnetotail. In *Abstract (SM13A-2769), presented at AGU24, 9-13 Dec 2024*. Retrieved from https://agu.confex.com/agu/agu24/meetingapp.cgi/Paper/1587780

Dubyagin, S., Sergeev, V., Apatenkov, S., Angelopoulos, V., Nakamura, R., McFadden, J., et al. (2010). Pressure and entropy changes in the flow-braking region during magnetic field dipolarization. *Journal of Geophysical Research*, *115*(A10), A10225. https://doi.org/10.1029/2010JA015625

Frank, L. A., Sigwarth, J. B., Craven, J. D., Cravens, J. P., Dolan, J. S., Dvorsky, M. R., et al. (1995). The visible imaging system (VIS) for the polar spacecraft. *Space Science Reviews*, *71*(1–4), 297–328. https://doi.org/10.1007/bf00751334

Fujii, R., Hoffman, R. A., Anderson, P. C., Craven, J. D., Sugiura, M., Frank, L. A., & Maynard, N. C. (1994). Electrodynamic parameters in the nighttime sector during auroral substorms. *Journal of Geophysical Research*, *99*(A4), 6093–6112. https://doi.org/10.1029/93JA02210

Fukushima, N., & Kamide, Y. (1973). Partial ring current models for worldwide geomagnetic disturbances. *Reviews of Geophysics*, *11*(4), 795–853. https://doi.org/10.1029/RG011i004p00795

Gjerloev, J. W., & Hoffman, R. A. (2014). The large-scale current system during auroral substorms. *Journal of Geophysical Research: Space Physics*, *119*(6), 4591–4606. https://doi.org/10.1002/2013JA019176

Kepko, L., McPherron, R. L., Amm, O., Apatenkov, S., Baumjohann, W., Birn, J., et al. (2015). Substorm current wedge revisited. *Space Science Reviews*, *190*(1–4), 1–46. https://doi.org/10.1007/s11214-014-0124-9

Kim, H.-S., Lee, D.-Y., Ohtani, S., Park, M.-Y., & Ahn, B.-H. (2012). On near-tail bubble penetration into geosynchronous altitude. *Journal of Geophysical Research*, *117*(A7), A07205. https://doi.org/10.1029/2012JA017749

Kokubun, S., Yamamoto, T., Acuna, M. H., Hayashi, K., Shiokawa, K., & Kawano, H. (1994). The geotail magnetic field experiment. *Journal of Geomagnetism and Geoelectricity*, *46*(1), 7–21. https://doi.org/10.5636/jgg.46.7

Lui, A. T. Y. (1991). Extended consideration of a synthesis model for magnetospheric substorms. *Geophysical Monograph Series*, *64*, 43–60. https://doi.org/10.1029/GM064p0043

Merkin, V. G., Panov, E. V., Sorathia, K., & Ukhorskiy, A. Y. (2019). Contribution of bursty bulk flows to the global dipolarization of the magnetotail during an isolated substorm. *Journal of Geophysical Research: Space Physics*, *124*(11), 8647–8668. https://doi.org/10.1029/2019JA026872

Motoba, T., Ohtani, S., Gkioulidou, M., Ukhorskiy, A. Y., Lanzerotti, L. J., & Claudepierre, S. G. (2021). Superposed epoch analysis of dispersionless particle injections inside geosynchronous orbit. *Journal of Geophysical Research: Space Physics*, *126*(8), e2021JA029546. https://doi.org/10.1029/2021JA029546

Mukai, T., Machida, S., Saito, Y., Hirahara, M., Terasawa, T., Kaya, N., et al. (1994). The low energy particle (LEP) experiment onboard the Geotail satellite. *Journal of Geomagnetism and Geoelectricity*, *46*(8), 669–692. https://doi.org/10.5636/jgg.46.669

Nagai, T. (1982). Observed magnetic substorm signatures at synchronous altitude. *Journal of Geophysical Research*, *87*(A6), 4405–4417. https://doi.org/10.1029/JA087iA06p04405

Newell, P. T., & Gjerloev, J. W. (2011). Evaluation of SuperMAG auroral electrojet indices as indicators of substorms and auroral power. *Journal of Geophysical Research*, *116*(A12), A12211. https://doi.org/10.1029/2011JA016779

Newell, P. T., & Gjerloev, J. W. (2012). SuperMAG-based partial ring current indices. *Journal of Geophysical Research*, *117*(A5), A05215. https://doi.org/10.1029/2012JA017586

Ohtani, S. (2021). Revisiting the partial ring current model: Longitudinal asymmetry of ground magnetic depression during geomagnetic storms. *Journal of Geophysical Research: Space Physics*, *126*(9), e2021JA029643. https://doi.org/10.1029/2021JA029643

Ohtani, S., Gjerloev, J. W., Anderson, B. J., Kataoka, R., Troshichev, O., & Watari, S. (2018). Dawnside wedge current system formed during intense geomagnetic storms. *Journal of Geophysical Research: Space Physics*, *123*(11), 9093–9109. https://doi.org/10.1029/2018JA025678

Ohtani, S., Imajo, S., Nakamizo, A., & Gjerloev, J. W. (2021). Globally correlated ground magnetic disturbances, during substorms. *Journal of Geophysical Research: Space Physics*, *126*(4), e2020JA028599. https://doi.org/10.1029/2020JA028599

Ohtani, S., Motoba, T., Gkioulidou, M., Takahashi, K., & Singer, H. J. (2018). Spatial development of the dipolarization region in the inner magnetosphere. *Journal of Geophysical Research: Space Physics*, *123*(7), 5452–5463. https://doi.org/10.1029/2018JA025443

Ohtani, S., & Mukai, T. (2008). Statistical characteristics of the storm time plasma sheet. *Journal of Geophysical Research*, *113*(A1). https://doi.org/10.1029/2007ja012547

Ohtani, S., Singer, H. J., & Mukai, T. (2006). Effects of the fast plasma sheet flow on the geosynchronous magnetic configuration: Geotail and GOES coordinated study. *Journal of Geophysical Research*, *111*(A1), A01204. https://doi.org/10.1029/2005JA011383

Ohtani, S., Sorathia, K., Merkin, V. G., Frey, H. U., & Gjerloev, J. W. (2023). External and internal causes of the stormtime intensification of the dawnside westward auroral electrojet. *Journal of Geophysical Research: Space Physics*, *128*, e2023JA031457. https://doi.org/10.1029/e2023JA031457

Raptis, S., Merkin, V., Ohtani, S., Gkioulidou, M., & Regoli, L. H. (2024). Plasma sheet magnetic flux transport during geomagnetic storms. *Geophysical Research Letters*, *51*(18), e2024GL110839. https://doi.org/10.1029/2024GL110839

Sergeev, V. A., Angelopoulos, V., Gosling, J. T., Cattell, C. A., & Russell, C. T. (1996). Detection of localized, plasma-depleted flux tubes or bubbles in the midtail plasma sheet. *Journal of Geophysical Research*, *101*(A5), 10817–10826. https://doi.org/10.1029/96JA00460

Shiokawa, K., Baumjohann, W., Haerendel, G., Paschmann, G., Fennell, J. F., Friis-Christensen, E., et al. (1998). High-speed ion flow, substorm current wedge, and multiple Pi 2 pulsations. *Journal of Geophysical Research*, *103*(A3), 4491–4507. https://doi.org/10.1029/97JA01680

Sorathia, K. A., Michael, A., Merkin, V. G., Ohtani, S., Keesee, A. M., Sciola, A., et al. (2023). Multiscale magnetosphere-ionosphere coupling during stormtime: A case study of the dawnside current wedge. *Journal of Geophysical Research: Space Physics*, *128*(11), e2023JA031594. https://doi.org/10.1029/2023JA031594

Tsyganenko, N. A., & Fairfield, D. H. (2004). Global shape of the magnetotail current sheet as derived from Geotail and Polar data. *Journal of Geophysical Research*, *109*(A3), A03218. https://doi.org/10.1029/2003JA010062

Weimer, D. R. (2005). Improved ionospheric electrodynamic models and application to calculating Joule heating rates. *Journal of Geophysical Research*, *110*(A5), A05306. https://doi.org/10.1029/2004JA010884

Wiltberger, M., Merkin, V., Lyon, J. G., & Ohtani, S. (2015). High-resolution global magnetohydrodynamic simulation of bursty bulk flows. *Journal of Geophysical Research: Space Physics*, *120*(6), 4555–4566. https://doi.org/10.1002/2015JA021080

Wolf, R. A., Wan, Y., Xing, X., Zhang, J.-C., & Sazykin, S. (2009). Entropy and plasma sheet transport. *Journal of Geophysical Research*, *114*(A9), A00D05. https://doi.org/10.1029/2009JA014044